Article

Processing and Investigation of $Cd_{0.5}Zn_{0.5}Fe_{2-x}Cr_xO_4$ $(0 \leq x \leq 2)$ Spinel Nanoparticles

Reem Khalid Alharbi [1,*], Noura Kouki [1,*], Abdulrahman Mallah [1], Lotfi Beji [2,*], Haja Tar [1], Azizah Algreiby [1], Abrar S. Alnafisah [1] and Sobhi Hcini [3]

[1] Department of Chemistry, College of Science, Qassim University, Buraydah 51452, Saudi Arabia; a.mallah@qu.edu.sa (A.M.); h.tar@qu.edu.sa (H.T.); grieby@qu.edu.sa (A.A.); alnafisaha@qu.edu.sa (A.S.A.)
[2] Department of Physics, College of Sciences and Arts at ArRass, Qassim University, Buraidah 51452, Saudi Arabia
[3] Faculty of Science and Technology of Sidi Bouzid, University Campus Agricultural City, University of Kairouan, Sidi Bouzid 9100, Tunisia; hcini_sobhi@yahoo.fr
[*] Correspondence: 411200348@qu.edu.sa (R.K.A.); n.kouki@qu.edu.sa (N.K.); l.beji@qu.edu.sa (L.B.)

Abstract: This study presents the synthesis of $Cd_{0.5}Zn_{0.5}Fe_{2-x}Cr_xO_4$ nanoparticles via the sol–gel method, along with a comprehensive characterization of their morphological, structural, infrared, and magnetic properties. The X-ray diffraction pattern confirms the formation of the spinel structure, and the cation distribution is estimated using X-ray analysis and confirmed by magnetization measurements. The crystalline size, ranging from 152 to 189 nm, and lattice parameter, varying from 8.51134 Å to 8.42067 Å, decrease with increasing Cr content. The saturation magnetization decreases from 55 emu/g to 10.8 emu/g, while the remanent magnetization increases ($3.5 \text{ emu/g} \leq M_r \leq 6.27 \text{ emu/g}$), and the coercivity increases ($82 \text{ Oe} \leq H_C \leq 422.15 \text{ Oe}$) with the addition of Cr ions. Fourier transform infrared (FTIR) spectroscopy reveals two absorption bands at ν_1 and ν_2, located near 600 and 400 cm^{-1}, respectively, which correspond to the vibrations of the metal–oxygen bonds in the spinel structure.

Keywords: spinels; sol–gel method; XRD; FTIR; SEM; magnetic properties

1. Introduction

Ferrites with spinel structures of MFe_2O_4 (M = Cd, Zn, Ni, and Co) are among the most extensively investigated oxides in recent years. Physico-chemical investigations of these materials have drawn upon various disciplines, including magnetism, optics, electronics, and mechanics. These materials, which can exist as nanoparticles, aggregates, and nanostructured powders consisting of grains separated by grain boundaries, offer distinct advantages for manipulation and utilization in various applications, such as recording heads, antenna rods, loading coils, microwave devices, and core materials for power transformers in electronics and telecommunication applications [1–3].

Numerous synthesis techniques, such as electrochemical [4], hydrothermal [5], co-precipitation [6], sol–gel [7], plasma synthesis [8], citrate precursor [9], and reverse micelle [10] techniques, have been developed to produce ferrite materials. Among these methods, the sol–gel route is an efficient technique due to its simplicity and ability to regulate the properties of the final product, leading to a homogeneous material with a stoichiometric composition and nanoscale grain size [11–14]. The sol–gel method enables the adjustment of various parameters to enhance the physical and chemical characteristics of spinel ferrites, including pH, citric acid content, calcination temperature, and grain size [11,12].

Scientists can change ferrite materials by adding different ions or using different processes to make them better for specific uses. For example, the substitution of Cr^{3+} can improve magnetic properties like remanence magnetization and coercivity, which are

essential for technology [15]. When natural chromite materials form in an environment with oxygen, they can mix Fe^{2+} and Fe^{3+} in different places, affecting their properties [16]. Lee and other researchers have studied how magnetic properties change when Cr^{3+} is substituted and found that magnetic moment and Curie temperature decrease with this substitution [17]. Other researchers have also looked at what happens when Fe^{3+} is replaced by Cr^{3+} [18,19]. The effect of Al^{3+} and Cr^{3+} substitution in cobalt ferrite has also been reported [20,21]. It was observed that substituting Al^{3+} and Cr^{3+} ions in the cobalt ferrite lattice leads to a decrease in the saturation magnetization values due to the lower magnetic moment of Al^{3+} and Cr^{3+} compared to Fe^{3+} ions.

Due to their potential applications, the Cd-Zn ferrites have gained significant attention in nanoscience and nanotechnology [22]. Various compositions of Cd-Zn ferrites have been extensively investigated and characterized in the literature [23–27], showing intriguing electrical, magnetic, and optical properties. Enhancing their properties is of great interest given the numerous applications of Cd-Zn ferrites. To this end, mixed Cd-Zn ($Cd_{0.5}Zn_{0.5}Fe_{2-x}Cr_xO_4$ with x ranging from 0 to 2) ferrites substituted with Cr were examined in this work. Equal concentrations of Cd and Zn were maintained. Cr^{3+} ions preferentially occupy the octahedral B-sites in $Cd_{0.5}Zn_{0.5}Fe_{2-x}Cr_xO_4$ ferrites, leading to their selection. The substitution of Fe^{3+} ions by Cr^{3+} ions with a different ionic radius alters the crystal geometry and modifies the materials' magnetic and dielectric characteristics. In this study, we report the synthesis of $Cd_{0.5}Zn_{0.5}Fe_{2-x}Cr_xO_4$ ($0 \leq x \leq 2$) samples using the sol–gel method and their morphological and structural characterization. In addition, the infrared and magnetic properties at room temperature were investigated. Our results showed that the prepared $Cd_{0.5}Zn_{0.5}Fe_{2-x}Cr_xO_4$ materials maintained a regular spinel cubic structure. These samples present several advantages, such as their good infrared and magnetic properties, low cost, and, above all, their easy synthesis. These features make the $Cd_{0.5}Zn_{0.5}Fe_{2-x}Cr_xO_4$ spinels a good candidate for magnetic devices and can be studied in perspective for other potential applications.

2. Experimental Section

2.1. Materials Synthesis

Cadmium, zinc, iron, and chromium nitrates were precursors to synthesize $Cd_{0.5}Zn_{0.5}Fe_{2-x}Cr_xO_4$ ($0 \leq x \leq 2$) nanoparticles. Stoichiometric amounts of the nitrates were weighed and dissolved in distilled water, which was heated to 90 °C. The metal cations were complexed with citric acid, which was added to each solution. Next, the pH was adjusted to around seven by adding ammonia to the solutions. Ethylene glycol, a polymerization agent, was added at this stage. After approximately 4 h, a viscous liquid (gel) began to form. To create a soft powder, the magnetic stirring temperature gradually increased to 250 °C. After grinding and annealing in the air for 12 h, the powders were subjected to an annealing temperature range of 700 °C to 1200 °C. All characterizations of $Cd_{0.5}Zn_{0.5}Fe_{2-x}Cr_xO_4$ spinels annealed at 1200 °C are presented in this study.

2.2. Materials Characterization Technics

The samples' X-ray diffraction (XRD) patterns were collected using the "Panalytical X'Pert Pro System" diffractometer, operating at a copper wavelength of 1.5406 Å. The measurements ranged from 10° to 80° with a step size of 0.02° and a counting period of 18 s per step. The morphology of the materials in the form of pellets was studied using Philips XL 30 scanning electron microscopy (SEM) equipped with an electron gun and a 15 kV accelerating voltage. The FTIR spectra in a wavenumber range of 400–1000 cm^{-1} were recorded using a Shimadzu Fourier Transform Infrared Spectrophotometer (FTIR-8400S).

3. Results and Discussions

3.1. SEM Micrographs

The samples were characterized using scanning electron microscopy (SEM). The resulting images and their corresponding grain size distributions are shown in Figure 1a–e.

The microscopic structure and morphology of $Cd_{0.5}Zn_{0.5}Fe_{2-x}Cr_xO_4$ with Cr substitution were also investigated. The SEM images revealed that the synthesized materials comprised an irregularly shaped group of tailed grains with a non-uniform grain size distribution. The particles exhibited a prismatic and pyramidal morphology.
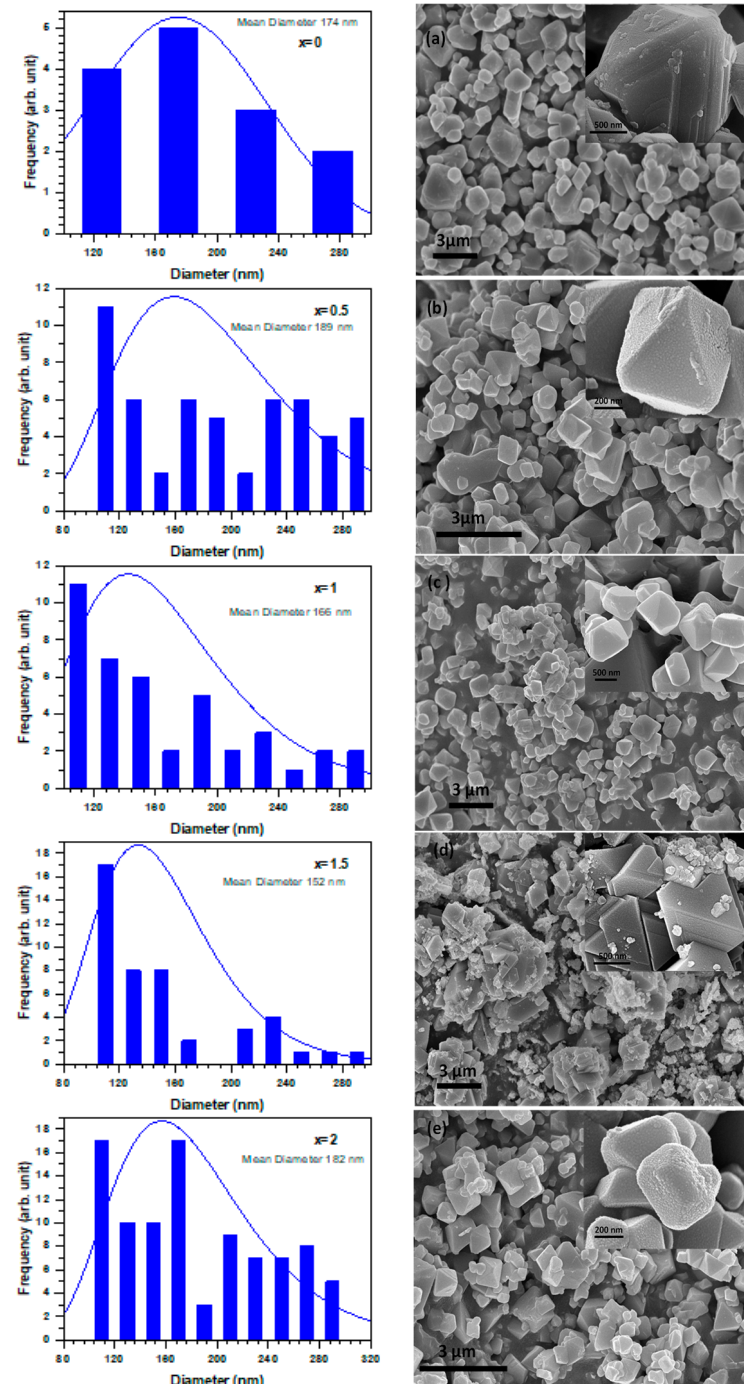

Figure 1. SEM micrographs and particle size distributions of $Cd_{0.5}Zn_{0.5}Fe_{2-x}Cr_xO_4$ spinels, elaborated by sol–gel method. Images labeled (**a–e**) correspond to x = 0, 0.5, 1, 1.5, and 2 Cr compositions, respectively. The inset images are the higher magnifications of micrographs.

Moreover, they were non-uniformly distributed, agglomerated, and inhomogeneous. Some massive particles were observed, along with smaller particles and increased agglomeration. All samples' average grain size values varied from 152 nm to 189 nm and were found to be random with a high Cr content [28,29].

3.2. Structural Properties and Cation Distributions

The XRD patterns of $Cd_{0.5}Zn_{0.5}Fe_{2-x}Cr_xO_4$ ferrites in Figure 2 reveal that a cubic spinel structure occurs in one phase. All diffraction lines are indexed in the cubic spinel structure, indicating the well-crystalline nature of the compounds. In addition, the absence of any reflection peak related to secondary phases confirms the purity of the samples. The cation distribution in the system was determined based on previous studies [30]. Mössbauer spectroscopic investigations have determined the cation distribution in ferrites with the general formula AB_2O_4. An investigation of Cd-Zn ferrites [24] and Cr-substituted ferrites [25] revealed that the tetrahedral A-sites were preferably occupied by Cd^{2+} and Zn^{2+} ions. In contrast, Cr^{3+} ions are distributed over the octahedral B-sites, and Fe^{3+} ions are distributed over both sites. This cation distribution has been confirmed in other studies [31,32]. Hence, the Rietveld refinement for $Cd_{0.5}Zn_{0.5}Fe_{2-x}Cr_xO_4$ samples was performed using the $\left(Cd_{0.5}^{2+}Zn_{0.5}^{2+}\right)_A\left[Fe_{2-x}^{3+}Cr_x^{3+}\right]_B O_4^{2-}$ cation distribution model. In this cation distribution, the A-sites are completely occupied by both Cd^{2+} and Zn^{2+} cations with equal concentrations (50 atom%). Hence, in the case of our samples, the Fe^{3+} and Cr^{3+} ions are distributed only over the octahedral B-sites. Furthermore, this cation distribution model confirms the absence of the inversion phenomenon and the non-occupation of the A-site by Fe^{3+} cations [33]. Figure 3 shows a typical example of the Rietveld refinement of $Cd_{0.5}Zn_{0.5}Fe_{2-x}Cr_xO_4$ spinel (x = 2). Table 1 outlines the various properties of the prepared compositions. The reliability factors (Bragg R_{Bragg}, profile R_p, experimental R_{exp}, and weighted profile R_{wp}) are all less than 10% in all cases. Rietveld fittings tend to be good, as shown by the $\chi^2 = R_{wp}/R_{exp}$ (goodness of fit) tendency towards unity. As a result, the refined occupancy factors for (Cd/Zn) and (Fe/Cr) at the A- and B-sites corresponded with the nominal values, supporting the suggested hypothesis. According to Table 1 and Figure 4, the decrease in lattice constant (a) and volume (V) appears to be caused by the replacement of a smaller radius of the Cr^{3+} ($r_{Cr}^{3+} = 0.63$Å) ion for the Fe^{3+} ion radius ($r_{Fe}^{3+} = 0.67$Å) [34]. Moreover, other Cr-doped ferrites have shown similar reductions in lattice parameters [35]. Furthermore, the atomic positions of oxygen exhibit the characteristic features of the spinel structure [13]. Alternatively, the cation–oxygen bond at the octahedral sites (d_{B-O}) is shorter with Cr substitution because of the decrease in the average ionic radius of the B-site $<r_B>$. Since the ionic radius of the A-site ($<r_A>$) remains the same, the length of the cation–oxygen bonds (d_{A-O}) remains almost constant. Table 1 also shows the bond angle values (φ_{A-O-B}) associated with A-O-B interactions in the produced samples. The bond angle for A-O-B is greater than that of B-O-B, according to Table 1. Thus, A-B exchange interactions are more potent than B-B exchange interactions [36,37]. Furthermore, the observed decrease in the bond angle (φ_{A-O-B}) indicates that A-B exchange interactions become less intense when Cr replacement is conducted. The XRD density was calculated using the following formula [14]:

$$d_x = \frac{8M}{Na^3} \tag{1}$$

where M is the molar mass, a is the cell parameter, and N is the Avogadro number (6.022×10^{23}). Table 1 (also Figure 4) shows that the XRD density increases with Cr substitution. This finding is consistent with previous reports in the literature [38]. The increase in XRD density may be due to the reduction in oxygen vacancies, which significantly impact densification kinetics [29]. It can also be attributed to the dominant effect of the reduction in the lattice parameter compared to the relatively small variation in molar mass resulting from the lower molar mass of Cr^{3+} ions (51.996 g/mol) compared to Fe^{3+} ions (55.847 g/mol).

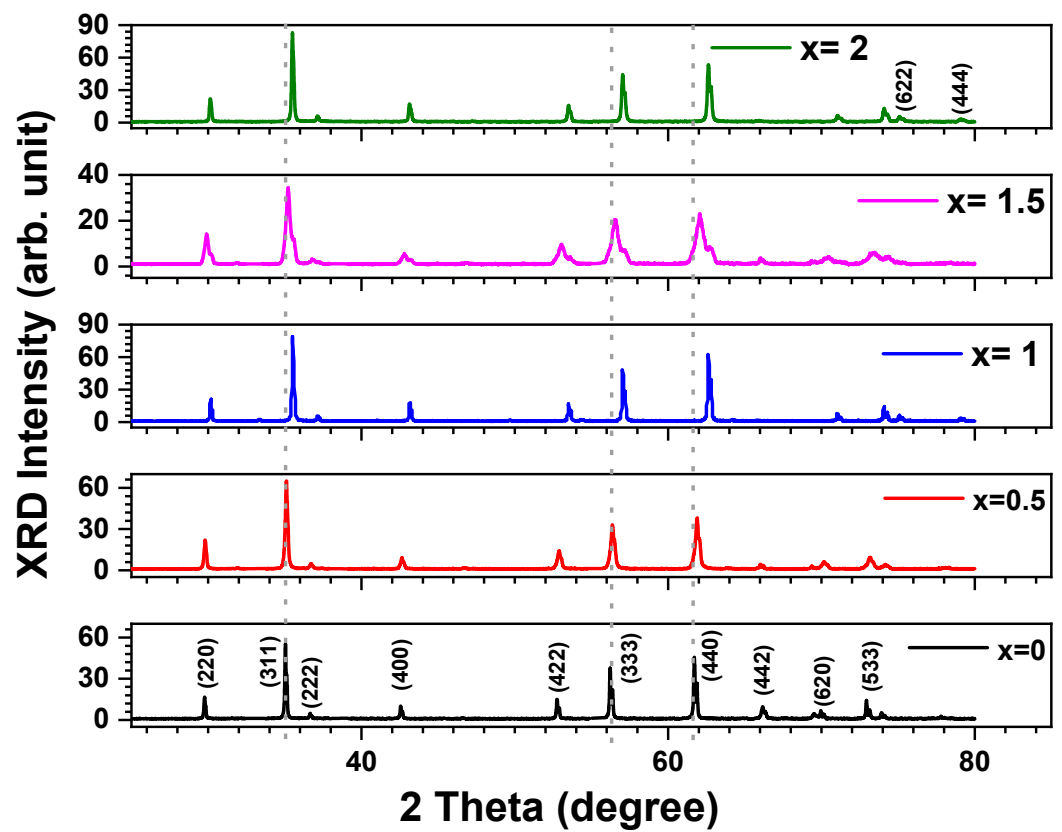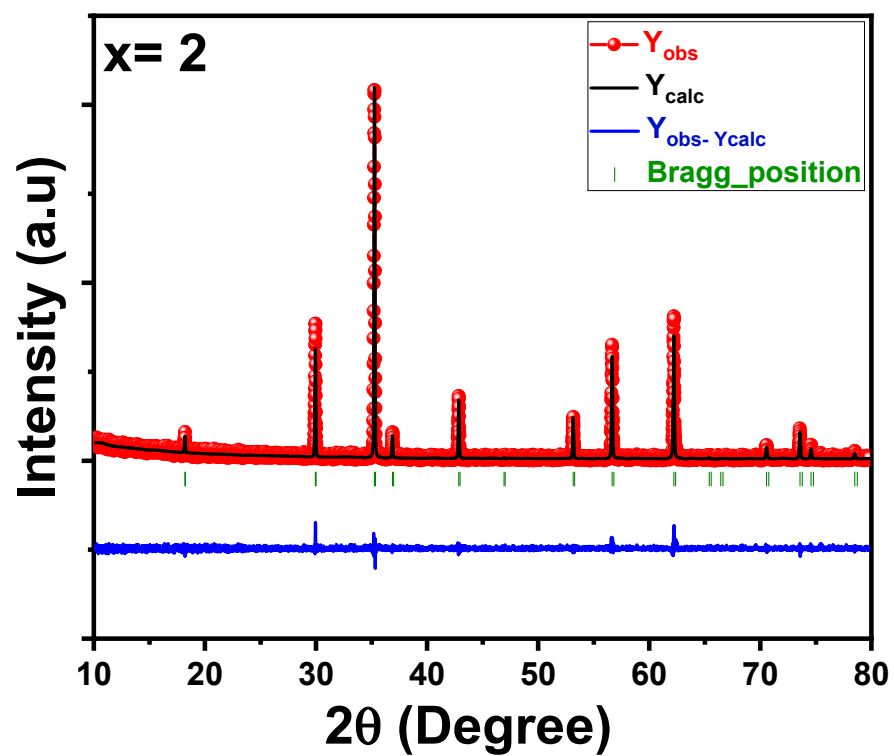**Figure 2.** XRD patterns of $Cd_{0.5}Zn_{0.5}Fe_{2-x}Cr_xO_4$ spinels with ($0 \leq x \leq 2$).

Figure 3. Typical example for the structural refinement of the XRD patterns using the Rietveld method for $Cd_{0.5}Zn_{0.5}Fe_{2-x}Cr_xO_4$ spinels with ($x = 2$).

Table 1. Structural parameters for $Cd_{0.5}Zn_{0.5}Fe_{2-x}Cr_xO_4$ spinels with ($0 \leq x \leq 2$) obtained following the structural refinement by the Rietveld method. a: cell parameter; V: cell volume; B_{iso}: isotropic thermal agitation parameter. Definitions of structural parameters are given in the text.

Cr Content			0	0.5	1	1.5	2
Space group			Fd$\bar{3}$m				
Cell parameters	a (Å)		8.5113 (4)	8.4745 (4)	8.4586 (4)	8.4395 (4)	8.4207 (4)
	V (Å^3)		616.59 (4)	608.61 (5)	605.20 (4)	601.10 (4)	597.09 (4)
Atoms	Tetrahedral A-site (Cd/Zn)	Wyckoff positions	4c	4c	4c	4c	4c
		Site symmetry	−43m	−43m	−43m	−43m	−43m
		Atomic positions x = y = z	1/8	1/8	1/8	1/8	1/8
		Occupancy factors	0.50 (1)/ 0.49 (1)	0.51 (1)/ 0.50 (1)	0.50 (1)/ 0.50 (1)	0.49 (1)/ 0.50 (1)	0.50 (1)/ 0.50 (1)
		B_{iso} (Å^2)	1.19	1.22	1.35	1.18	1.27
	Octahedral B-site [Fe/Cr]	Wyckoff positions	16d	16d	16d	16d	16d
		Site symmetry	−3m	−3m	−3m	−3m	−3m
		Atomic positions x = y = z	1/2	1/2	1/2	1/2	1/2
		Occupancy factors	2.01 (2)/ 0	1.51 (2)/0.49 (2)	1.01 (2)/1.02 (2)	0.50 (2)/1.48 (2)	0/2.02(2)
		B_{iso} (Å^2)	1.46	1.14	1.22	0.94	1.34
	O	Wyckoff positions	32e	32e	32e	32e	32e
		Site symmetry	3m	3m	32e	32e	32e
		Atomic positions x = y = z	0.2553 (1)	0.2551 (8)	0.2548 (8)	0.2545 (8)	0.2541 (8)
		Occupancy factors	4	4	4	4	4
		B_{iso} (Å^2)	1.42	1.54	1.42	1.65	1.58
Structural parameters	d_{A-O} (Å)		1.905 (8)	1.903 (7)	1.901 (9)	1.898 (7)	1.896 (8)
	d_{B-O} (Å)		2.058 (9)	2.053 (7)	2.045 (8)	2.041 (7)	2.036 (7)
	φ_{A-O-B} (°)		124.8 (5)	124.5 (3)	123.7 (4)	123.4 (3)	123.1 (3)
	φ_{B-O-B} (°)		92.4 (5)	91.2 (3)	91.0 (4)	90.8 (3)	90.3 (3)
	d_x (g. cm^{-3})		5.7004	5.7331	5.7443	5.7622	5.7795
Agreement factors	R_p (%)		6.41	5.47	5.44	5.63	5.48
	R_{wp} (%)		8.25	7.52	7.35	7.42	7.25
	R_{exp} (%)		7.14	7.33	7.47	7.12	7.04
	R_{Bragg} (%)		3.83	3.34	3.83	2.94	2.72
	χ^2 (%)		1.13	1.19	1.23	1.32	1.18

The values of the crystallite size (D_{XRD}) and the lattice strain (ε) were determined by the Williamson–Hall method as a function of Cr content. This method, developed by G.K. Williamson and his student W.H. Hall [39], utilizes the full width at half maximum (FWHM) of Bragg peaks ($\Delta\theta$, in radians) and the angle of peak position (θ), as well as the X-ray wavelength ($\lambda = 1.5406$ Å), to calculate the average crystallite size (D) and lattice strain (ε). The relationship is given by $\Delta\theta\cos\theta = \frac{k\lambda}{D} + 4\varepsilon\sin\theta$, where k is a constant value (0.94) obtained by assuming the spherical nature of the powders. By plotting $\Delta\theta \times \cos\theta$ versus $4\sin\theta$, the strain component (ε) can be determined from the slope, and the size component can be determined from the intercept ($\frac{k\lambda}{D}$). This plot is known as a Williamson–Hall plot. Figure 5a–e depicts the variations in $((\Delta\theta_{hkl})\cos\theta_{hkl})$ as a function of $(4\sin\theta_{hkl})$ for $Cd_{0.5}Zn_{0.5}Fe_{2-x}Cr_xO_4$ spinels (x = 0; x = 0.5; x = 1; x = 1.5; x = 2). The estimated values

of D_{XRD} and ε are (150 nm, 1.93×10^{-4}), (120 nm, 1.12×10^{-3}), (103 nm, 1.32×10^{-4}), (108 nm, 3.10×10^{-3}), and (95 nm, 3.4×10^{-3}) for $Cd_{0.5}Zn_{0.5}Fe_{2-x}Cr_xO_4$ spinels (x = 0; x = 0.5; x = 1; x = 1.5; x = 2), respectively. These results suggest a small variation in crystallite size due to Cr substitution, consistent with the values obtained from SEM analysis. The lattice strain increases while the crystallite size decreases approximately with an increasing Cr content.
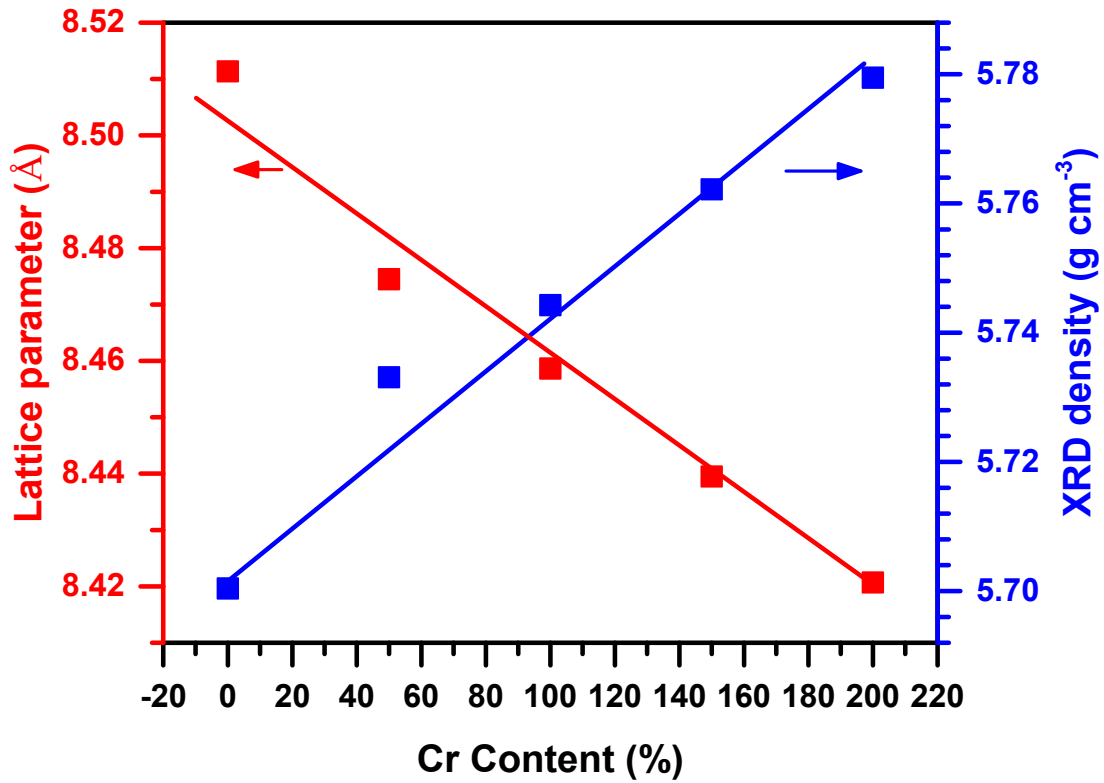

Figure 4. Lattice parameter and XRD density of $Cd_{0.5}Zn_{0.5}Fe_{2-x}Cr_xO_4$ ($0 \leq x \leq 2$) spinels as a function of Cr content.
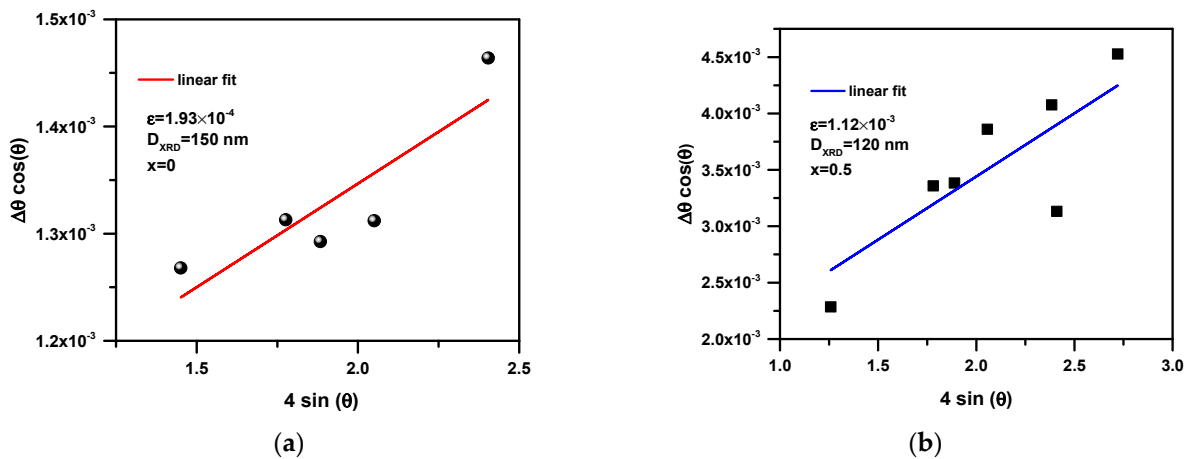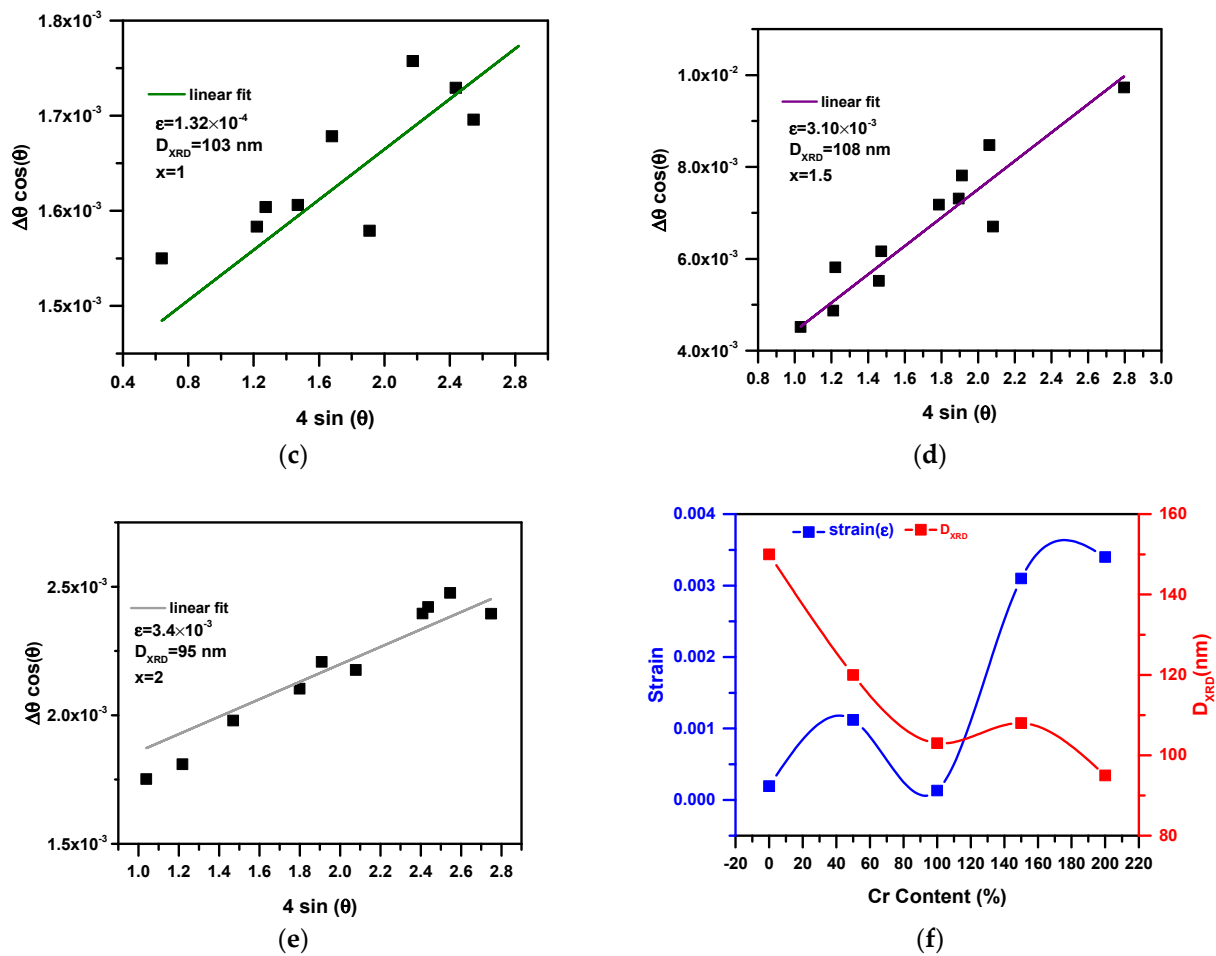

(**a**)

(**b**)

Figure 5. *Cont.*

Figure 5. (**a**–**e**) Williamson–Hall plots of ($\Delta\theta\cos\theta$) vs. ($4\sin\theta$) of $Cd_{0.5}Zn_{0.5}Fe_{2-x}Cr_xO_4$ spinels (x = 0; x = 0.5; x = 1; x = 1.5; x = 2). (**f**) Values of the crystallite's size (DXRD) and the lattice strain (ε) calculated using the Williamson–Hall methods.

3.3. FTIR Spectra

The infrared (IR) spectra provide valuable information about the crystal lattice's valence state and vibrational modes. Table 2 presents the band positions obtained from the IR spectra of the $Cd_{0.5}Zn_{0.5}Cr_xFe_{2-x}O_4$ series. Figure 6 shows the IR spectra of this series, with the high-frequency band υ_1 observed in the 524–586 cm^{-1} range and a small band in the low-frequency band υ_2 in the 420–424 cm^{-1} range. These absorption bands indicate the formation of a single-phase spinel structure. The two major absorption bands at υ_1 and υ_2 are due to vibrations of the oxygen bonds with positive ions at A- and B-sites [40]. The small band at low-frequency band υ_2 is constant for all samples except for x = 2, where it disappears. The vibrational bands υ_1 and υ_2 are assigned to intrinsic vibrations of the tetrahedral and octahedral sites, respectively [41].

Table 2. Band positions (υ_1 and υ_2) and force constants (K_O and K_T) of $Cd_{0.5}Zn_{0.5}Fe_{2-x}Cr_xO_4$.

x	υ_1	υ_2	$K_T \times 10^5$ (dyne cm^{-1})	$K_O \times 10^5$ (dyne cm^{-1})
0	524	423	1.86	1.06
0.5	569	424	2.19	1.05
1	584	421	2.31	1.02
1.5	586	420	2.33	1.01
2	586	420	2.33	1.00

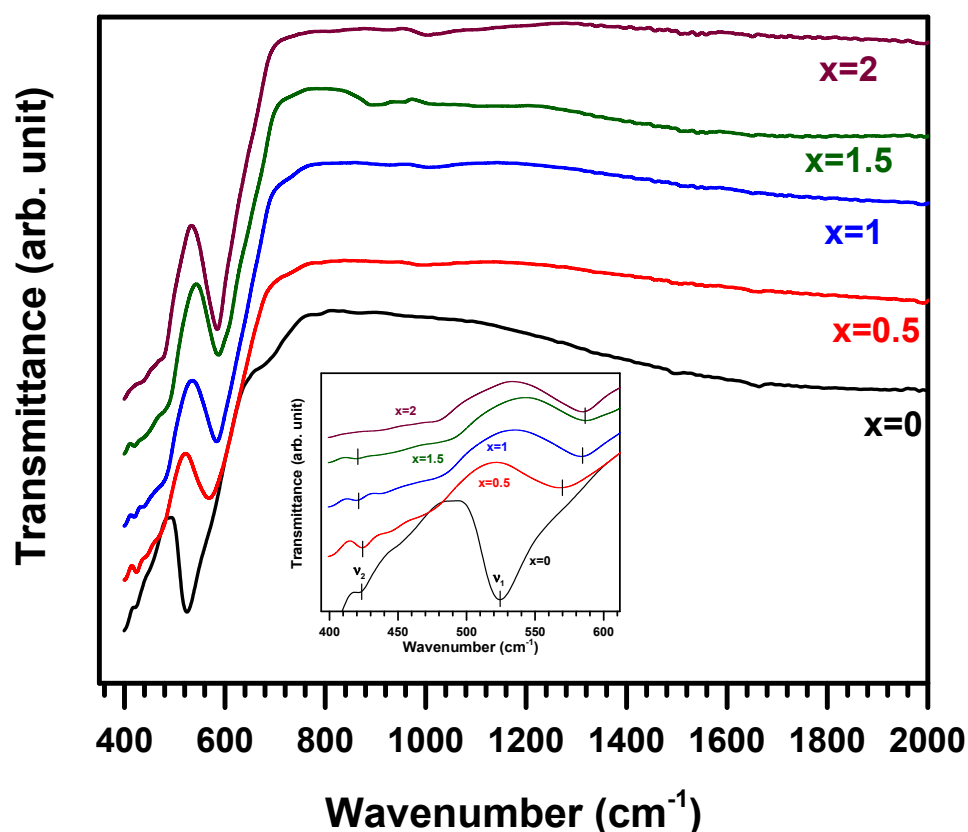**Figure 6.** FTIR spectra at room temperature of $Cd_{0.5}Zn_{0.5}Fe_{2-x}Cr_xO_4$ spinel ferrites. Spectra is vertically translated for more clarity details. The inset figure is the higher magnification of the region between 400 and 600 cm^{-1} represented in semi-log scale.

The infrared spectra of the Cr-substituted ferrite system prepared through the ceramic route exhibit similar features, as reported in the literature [42]. The intensity of the absorption band corresponding to the tetrahedral complex (υ_1) increases and shifts towards a higher frequency with an increased Cr content, while the octahedral complex (υ_2) exhibits weaker absorption bands. This behavior can be attributed to the first selection rule, which states that transitions between d orbitals in a complex with a center of symmetry are forbidden. As the tetrahedral complex possesses a center of symmetry, its absorption bands are more intense than those of the octahedral complex, which lacks a center of symmetry and thus allows more transitions to occur between d orbitals [43].

The observed shift in the band position in the IR spectra is attributed to the change in the Fe^{3+}-O_2^{2-} distance for the tetrahedral and octahedral complexes. The slight frequency change in band υ_2 and the significant shift of band υ_1 towards a higher frequency are due to the substitution of Cr^{3+} ions, which replace Fe^{3+} ions only at the octahedral B-site, leading to no significant change in the size of the octahedral site. As the Fe_B^{3+}-O_2^{2-} complex numbers decrease, metal–oxygen vibrational energies increase, prompting a decrease in the Fe_B^{3+}-O_2^{2-} intermolecular distance. This phenomenon is observed due to the increased number of Cr^{3+}-O_2^{2-} complexes [38] and the creation of $Me^{3+}O_2^{2-}$ complexes at A-sites. As Cd^{2+}-O^{2-} and Zn^{2+}-O^{2-} bonds are stretched at the A-sites and Fe^{3+}-O^{2-} and Cr^{3+}-O^{2-} bonds are stretched at the B-sites, these bands are produced. The two bands may exhibit different positions for various reasons, including differences in ionic radius, the average distance between metal and oxygen, and electronegativity. It has been found that similar results have been obtained for other ferrite systems [44–46]. Assuming that the other independent parameters are constant, the force constant would be the second derivative of the potential energy based on the site radius. Based on Waldron's method [41], we

calculated force constants for tetrahedral and octahedral sites. For each site, Waldron gives the force constants K_T and K_O as follows:

$$K_T = 7.62 M_1 v_1^2 10^{-3} \left(\frac{dyne}{cm} \right) \tag{2}$$

$$K_O = 10.62 \left(\frac{M_2}{2} \right) v_2^2 10^{-3} \left(\frac{dyne}{cm} \right) \tag{3}$$

Assuming that M_1 and M_2 refer to the molecular weight of the cations at sites A and B, respectively. Based on the cation distribution for the prepared samples, tetrahedral M_1 and octahedral M_2 molecular weights have been calculated. Table 2 contains the force constants K_T and K_O. With an increasing Cr content, force constants K_T and K_O increase. According to IR studies, bond length and the force constant inversely relate [47].

3.4. Magnetic Properties

To obtain the magnetic hysteresis curves, a magnetic field (± 50 kOe) is applied to the prepared samples at room temperature (see Figure 7). Samples at low magnetic fields exhibit nonlinear magnetization and become saturated at high magnetic fields, revealing ferromagnetism. Table 3 summarizes saturation magnetization (M_s), remanent magnetization (M_r), and coercivity (H_c) results. The synthesized samples have low H_c values. Therefore, the samples could be classified as soft magnetic spinels. As a result, the $Cd_{0.5}Zn_{0.5}Cr_xFe_{2-x}O_4$ spinels have the potential to be applied in some magnetic applications such as recording heads, spintronic devices, microwave devices, transformers, induction cores, telecommunication systems, electromagnetic devices, and magnetic recording field sensors [48–50]. As the Cr content increases, the H_c also increases, indicating an increase in the resistive nature against spin inversion. The anisotropy constant increases with an increasing Cr content but decreases when the Cr content is more significant than 0.5. The anisotropy constant K depends on the substituted ion concentration [51], which can be evaluated using the corresponding relation.

$$H_c = 0.98 \frac{K}{M_S} \tag{4}$$

Furthermore, saturation magnetization is related to H_c through Brown's relation [52], and $H_c = \frac{2K}{\mu_0 M_s}$, states that H_c is inversely proportional to M_s. This is consistent with our experimental results.

Table 3. Values of the spontaneous magnetization (M_s), remanent magnetization (M_r), coercivity (H_c), H_c magnetic field, and anisotropy constant K.

x.	M_r (emu/g)	M_s (emu/g)	H_c (Oe)	H_s	K (erg/cm^3)
0	3.5	55	82	4950	4602
0.5	8.2	37.8	237	4500	9141
1	9	27.45	311.35	4478	8536
1.5	10.8	17	402	4423	6973
2	6.27	10.8	422.15	4387	4652

Table 3 illustrates the decrease in the M_s value with Cr replacement, consistent with other spinel systems [53,54]. There is a correlation between the increase in M_s values and Neel's theory [55] and the cations distribution between A- and B-sites. According to Neel's model, ferrimagnet materials interact in three ways: A-A, B-B, and A-B sublattices. A-A and B-B interactions within the sublattice are dominated by the super-exchange interaction between A- and B-sites. Consequently, the net magnetic moment consists of the vector sum of magnetic moments on sublattices A and B [56]:

$$n_B^{cal} = |M_B - M_A| \tag{5}$$

M_B and M_A represent B and A sublattice magnetic moments in Bohr magneton (μ_B), respectively. When Cr^{3+} replaces Fe^{3+} at the octahedral site, saturation magnetization decreases since the Cr^{3+} ion (3 μ_B) has a smaller magnetic moment than Fe^{3+}(5 μ_B) [57]. Accordingly, the magnetic properties of the prepared samples are closely related to their predicted cation distribution.
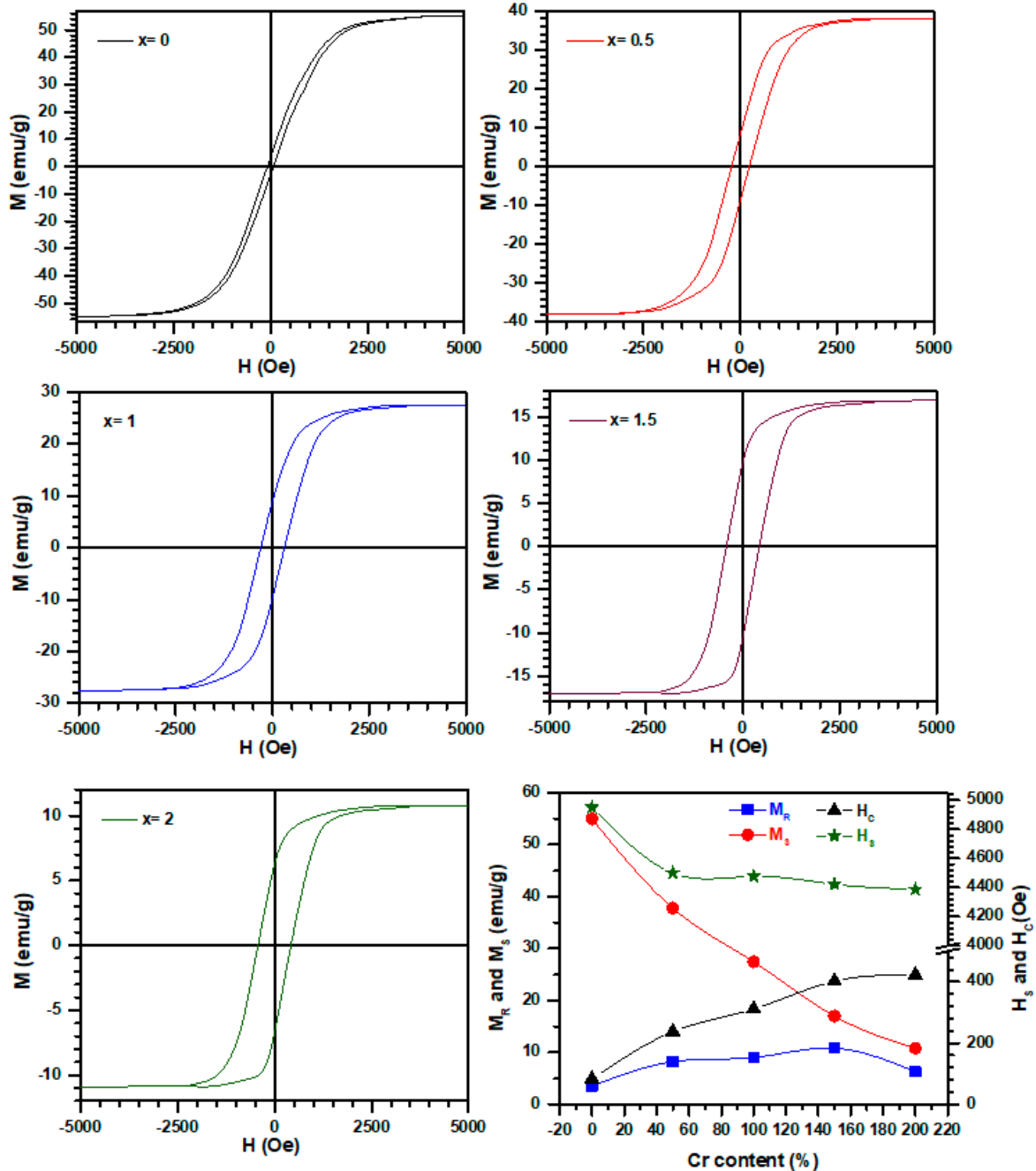

Figure 7. Magnetization loop M-H of $Cd_{0.5}Zn_{0.5}Fe_{2-x}Cr_xO_4$ spinels recorded at 300 K The values M_r, M_s, H_c, and H_s were extracted from M-H curves and plotted as a function of Cr content.

The inset of Figure 8 shows variations in the anisotropy constant "K" and static susceptibility "χ_S" with Cr. The ratio M_s/H_s, named static susceptibility χ_S, increases linearly with the Cr content. In contrast, the anisotropic coefficient increases with the Cr content. It reaches a maximum when the Cr composition is equal to that of Fe and regains the same value as the beginning ferrite when the material becomes chromite.
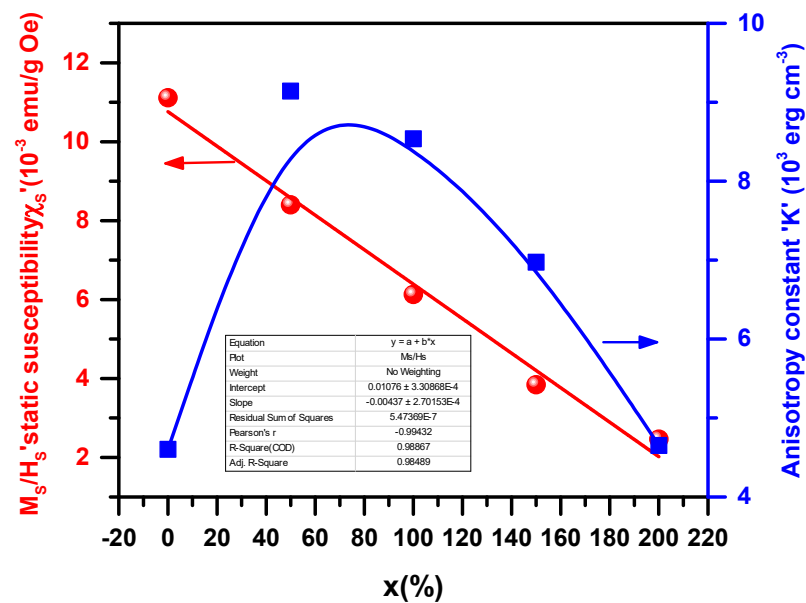
Equation	y = a + b*x
Plot	Ms/Hs
Weight	No Weighting
Intercept	0.01076 ± 3.30868E-4
Slope	-0.00437 ± 2.70153E-4
Residual Sum of Squares	5.47369E-7
Pearson's r	-0.99432
R-Square(COD)	0.98867
Adj. R-Square	0.98489

Figure 8. Variation in anisotropy constant "K" and static susceptibility ''χ_S'' with Cr content.

4. Conclusions

$Cd_{0.5}Zn_{0.5}Fe_{2-x}Cr_xO_4$ ($0 \leq x \leq 2$) ferrites synthesized via the sol–gel method exhibit a cubic Fd3m spinel structure. Substituting Cr for Fe reduces cell parameters, average grain size, spontaneous magnetization, and conductivity compared to the parent compound $Cd_{0.5}Zn_{0.5}Fe_2O_4$. The FTIR spectra reveal two principal absorption bands that increase with Cr substitution. These materials show potential for use in various magnetic and electronic applications. The significant findings of this work show that the examined materials have regular spinel cubic structures and low coercive fields, allowing them to be used in magnetic devices.

Author Contributions: Conceptualization, S.H., A.M. and L.B.; Methodology, R.K.A., N.K. and A.M.; Software, A.S.A. and H.T.; Formal analysis, L.B., S.H. and A.S.A.; Investigation, L.B. and S.H.; Writing—original draft, R.K.A., L.B., A.A., A.S.A. and S.H.; Writing—review & editing, N.K., A.A. and H.T.; Supervision, N.K. and A.M. All authors have read and agreed to the published version of the manuscript.

Data Availability Statement: Not applicable.

References

1. Adam, J.D.; Davis, L.E.; Dionne, G.F.; Schloemann, E.F.; Stitzer, S.N. Ferrite Devices and Materials. *IEEE Trans. Microw. Theory Tech.* **2002**, *50*, 721–737. [CrossRef]
2. Kulikowski, J. Soft Magnetic Ferrites—Development or Stagnation? *J. Magn. Magn. Mater.* **1984**, *41*, 56–62. [CrossRef]
3. Harris, V.G.; Geiler, A.; Chen, Y.; Yoon, S.D.; Wu, M.; Yang, A.; Chen, Z.; He, P.; Parimi, P.V.; Zuo, X. Recent Advances in Processing and Applications of Microwave Ferrites. *J. Magn. Magn. Mater.* **2009**, *321*, 2035–2047. [CrossRef]
4. Mazarío, E.; Herrasti, P.; Morales, M.P.; Menéndez, N. Synthesis and Characterization of CoFe2O4 Ferrite Nanoparticles Obtained by an Electrochemical Method. *Nanotechnology* **2012**, *23*, 355708. [CrossRef] [PubMed]
5. Chen, K.; Jia, L.; Yu, X.; Zhang, H. A Low Loss NiZnCo Ferrite, Prepared Using a Hydrothermal Method, for Antenna Applications. *J. Appl. Phys.* **2014**, *115*, 17A520. [CrossRef]
6. Rahman, S.; Nadeem, K.; Anis-ur-Rehman, M.; Mumtaz, M.; Naeem, S.; Letofsky-Papst, I. Structural and Magnetic Properties of ZnMg-Ferrite Nanoparticles Prepared Using the Co-Precipitation Method. *Ceram. Int.* **2013**, *39*, 5235–5239. [CrossRef]
7. Sun, L.; Zhang, R.; Ni, Q.; Cao, E.; Hao, W.; Zhang, Y.; Ju, L. Magnetic and Dielectric Properties of $Mg_xCo_{1-X}Fe_2O_4$ Ferrites Prepared by the Sol-Gel Method. *Phys. B Condens. Matter* **2018**, *545*, 4–11. [CrossRef]

8. Safari, A.; Gheisari, K.; Farbod, M. Structural, Microstructural, Magnetic and Dielectric Properties of Ni-Zn Ferrite Powders Synthesized by Plasma Arc Discharge Process Followed by Post-Annealing. *J. Magn. Magn. Mater.* **2019**, *488*, 165369. [CrossRef]

9. Soibam, I.; Phanjoubam, S.; Prakash, C. Mössbauer and Magnetic Studies of Cobalt Substituted Lithium Zinc Ferrites Prepared by Citrate Precursor Method. *J. Alloys Compd.* **2009**, *475*, 328–331. [CrossRef]

10. Singh, C.; Jauhar, S.; Kumar, V.; Singh, J.; Singhal, S. Synthesis of Zinc Substituted Cobalt Ferrites via Reverse Micelle Technique Involving in Situ Template Formation: A Study on Their Structural, Magnetic, Optical and Catalytic Properties. *Mater. Chem. Phys.* **2015**, *156*, 188–197. [CrossRef]

11. Hankare, P.P.; Jadhav, S.D.; Sankpal, U.B.; Chavan, S.S.; Waghmare, K.J.; Chougule, B.K. Synthesis, Characterization and Effect of Sintering Temperature on Magnetic Properties of MgNi Ferrite Prepared by Co-Precipitation Method. *J. Alloys Compd.* **2009**, *475*, 926–929. [CrossRef]

12. Ebrahimi, S.A.S.; Masoudpanah, S.M. Effects of PH and Citric Acid Content on the Structure and Magnetic Properties of MnZn Ferrite Nanoparticles Synthesized by a Sol–Gel Autocombustion Method. *J. Magn. Magn. Mater.* **2014**, *357*, 77–81. [CrossRef]

13. Kouki, N.; Hcini, S.; Boudard, M.; Aldawas, R.; Dhahri, A. Microstructural Analysis, Magnetic Properties, Magnetocaloric Effect, and Critical Behaviors of $Ni_{0.6}Cd_{0.2}Cu_{0.2}Fe_2O_4$ Ferrites Prepared Using the Sol–Gel Method under Different Sintering Temperatures. *RSC Adv.* **2019**, *9*, 1990–2001. [CrossRef] [PubMed]

14. Hcini, S.; Kouki, N.; Omri, A.; Dhahri, A.; Bouazizi, M.L. Effect of Sintering Temperature on Structural, Magnetic, Magnetocaloric and Critical Behaviors of Ni-Cd-Zn Ferrites Prepared Using Sol-Gel Method. *J. Magn. Magn. Mater.* **2018**, *464*, 91–102. [CrossRef]

15. Mane, D.R.; Patil, S.; Birajdar, D.D.; Kadam, A.B.; Shirsath, S.E.; Kadam, R.H. Sol–Gel Synthesis of Cr^{3+} Substituted $Li_{0.5}Fe_{2.5}O_4$: Cation Distribution, Structural and Magnetic Properties. *Mater. Chem. Phys.* **2011**, *126*, 755–760. [CrossRef]

16. Mitra, S.; Bidyananda, M.; Samanta, A.K. Cation Distribution in Cr-Spinels from the Sittampundi Layered Complex and Their Intracrystalline Thermodynamics. *Curr. Sci.* **2006**, *90*, 435–439.

17. Lee, S.H.; Yoon, S.J.; Lee, G.J.; Kim, H.S.; Yo, C.H.; Ahn, K.; Lee, D.H.; Kim, K.H. Electrical and Magnetic Properties of $NiCr_xFe_{2-X}O_4$ Spinel ($0 \leq X \leq 0.6$). *Mater. Chem. Phys.* **1999**, *61*, 147–152. [CrossRef]

18. Ikehara, T.; Yamaguchi, H.; Hosokawa, K.; Miyamoto, H.; Aizawa, K. Effects of ELF Magnetic Field on Membrane Protein Structure of Living HeLa Cells Studied by Fourier Transform Infrared Spectroscopy. *Bioelectromagn. J. Bioelectromagn. Soc. Soc. Phys. Regul. Biol. Med. Eur. Bioelectromagn. Assoc.* **2003**, *24*, 457–464. [CrossRef]

19. Gismelseed, A.M.; Yousif, A.A. Mössbauer Study of Chromium-Substituted Nickel Ferrites. *Phys. B Condens. Matter* **2005**, *370*, 215–222. [CrossRef]

20. Singhal, S.; Sharma, R.; Namgyal, T.; Jauhar, S.; Bhukal, S.; Kaur, J. Structural, Electrical and Magnetic Properties of $Co_{0.5}Zn_{0.5}Al_xFe_{2-X}O_4$ (X = 0, 0.2, 0.4, 0.6, 0.8 and 1.0) Prepared via Sol–Gel Route. *Ceram. Int.* **2012**, *38*, 2773–2778. [CrossRef]

21. Singhal, S.; Jauhar, S.; Singh, J.; Chandra, K.; Bansal, S. Investigation of Structural, Magnetic, Electrical and Optical Properties of Chromium Substituted Cobalt Ferrites ($CoCr_xFe_{2-X}O_4$, $0 \leq X \leq 1$) Synthesized Using Sol Gel Auto Combustion Method. *J. Mol. Struct.* **2012**, *1012*, 182–188. [CrossRef]

22. Valan, M.F.; Manikandan, A.; Antony, S.A. Microwave Combustion Synthesis and Characterization Studies of Magnetic $Zn_{1-x}Cd_xFe_2O_4$ ($0 \leq X \leq 0.5$) Nanoparticles. *J. Nanosci. Nanotechnol.* **2015**, *15*, 4543–4551. [CrossRef] [PubMed]

23. Harish, K.N.; Naik, H.S.B.; Viswanath, R. Synthesis, Enhanced Optical and Photocatalytic Study of Cd–Zn Ferrites under Sunlight. *Catal. Sci. Technol.* **2012**, *2*, 1033–1039. [CrossRef]

24. Gupta, M.; Gupta, M.; Mudsainiyan, R.K.; Randhawa, B.S. Physico-Chemical Analysis of Pure and Zn Doped Cd Ferrites ($Cd_{1-X}Zn_xFe_2O_4$) Nanofabricated by Pechini Sol–Gel Method. *J. Anal. Appl. Pyrolysis* **2015**, *116*, 75–85. [CrossRef]

25. Chakrabarti, M.; Sanyal, D.; Chakrabarti, A. Preparation of $Zn_{(1-x)}Cd_xFe_2O_4$ (X = 0.0, 0.1, 0.3, 0.5, 0.7 and 1.0) Ferrite Samples and Their Characterization by Mössbauer and Positron Annihilation Techniques. *J. Phys. Condens. Matter* **2007**, *19*, 236210. [CrossRef]

26. Siddique, M.; Anwar-ul-Islam, M.; Butt, N.M.; Abbas, T. Composition Dependence of Quadrupole Splitting in Cd—Zn Ferrites. *Phys. Status Solidi* **1999**, *216*, 1069–1072. [CrossRef]

27. Arean, C.O.; Diaz, E.G.; Gonzalez, J.M.R.; Garcia, M.A.V. Crystal Chemistry of Cadmium-Zinc Ferrites. *J. Solid State Chem.* **1988**, *77*, 275–280. [CrossRef]

28. Weil, L.; Bertaut, F.; Bochirol, L. Propriétés Magnétiques et Structure de La Phase Quadratique Du Ferrite de Cuivre. *J. Phys. le Radium* **1950**, *11*, 208–212. [CrossRef]

29. Mane, D.R.; Birajdar, D.D.; Shirsath, S.E.; Telugu, R.A.; Kadam, R.H. Structural and Magnetic Characterizations of Mn—Ni—Zn Ferrite Nanoparticles. *Phys. Status Solidi* **2010**, *207*, 2355–2363. [CrossRef]

30. Cvejic, Z.; Rakic, S.; Kremenovic, A.; Antic, B.; Jovalekic, C.; Colomban, P. Nanosize Ferrites Obtained by Ball Milling: Crystal Structure, Cation Distribution, Size-Strain Analysis and Raman Investigations. *Solid State Sci.* **2006**, *8*, 908–915. [CrossRef]

31. Hakim, M.A.; Nath, S.K.; Sikder, S.S.; Maria, K.H. Cation Distribution and Electromagnetic Properties of Spinel Type Ni–Cd Ferrites. *J. Phys. Chem. Solids* **2013**, *74*, 1316–1321. [CrossRef]

32. Khalaf, K.A.M.; Al Rawas, A.D.; Gismelssed, A.M.; Al Jamel, A.; Al Ani, S.K.J.; Shongwe, M.S.; Al Riyami, K.O.; Al Alawi, S.R. Influence of Cr Substitution on Debye-Waller Factor and Related Structural Parameters of $ZnFe_{2-X}Cr_xO_4$ Spinels. *J. Alloys Compd.* **2017**, *701*, 474–486. [CrossRef]

33. Hossain, A.K.M.A.; Mahmud, S.T.; Seki, M.; Kawai, T.; Tabata, H. Structural, Electrical Transport, and Magnetic Properties of $Ni_{1-X}Zn_xFe_2O_4$. *J. Magn. Magn. Mater.* **2007**, *312*, 210–219. [CrossRef]

34. Shannon, R.D. Revised Effective Ionic Radii and Systematic Studies of Interatomic Distances in Halides and Chalcogenides. *Acta Crystallogr. Sect. A Cryst. Phys. Diffr. Theor. Gen. Crystallogr.* **1976**, *32*, 751–767. [CrossRef]

35. Patange, S.M.; Shirsath, S.E.; Lohar, K.S.; Algude, S.G.; Kamble, S.R.; Kulkarni, N.; Mane, D.R.; Jadhav, K.M. Infrared Spectral and Elastic Moduli Study of $NiFe_{2-X}Cr_XO_4$ Nanocrystalline Ferrites. *J. Magn. Magn. Mater.* **2013**, *325*, 107–111. [CrossRef]

36. Kumar, G.; Kotnala, R.K.; Shah, J.; Kumar, V.; Kumar, A.; Dhiman, P.; Singh, M. Cation Distribution: A Key to Ascertain the Magnetic Interactions in a Cobalt Substituted Mg–Mn Nanoferrite Matrix. *Phys. Chem. Chem. Phys.* **2017**, *19*, 16669–16680. [CrossRef]

37. Sharma, R.; Thakur, P.; Kumar, M.; Thakur, N.; Negi, N.S.; Sharma, P.; Sharma, V. Improvement in Magnetic Behaviour of Cobalt Doped Magnesium Zinc Nano-Ferrites via Co-Precipitation Route. *J. Alloys Compd.* **2016**, *684*, 569–581. [CrossRef]

38. Hemeda, O.M.; Amer, M.A.; Aboul-Enein, S.; Ahmed, M.A. Effect of Sintering on X-Ray and IR Spectral Behaviour of the $MnAl_xFe_{2-x}O_4$ Ferrite System. *Phys. Status Solidi* **1996**, *156*, 29–38. [CrossRef]

39. Williamson, G.K.; Hall, W.H. X-Ray Line Broadening from Filed Aluminium and Wolfram. *Acta Metall.* **1953**, *1*, 22–31. [CrossRef]

40. AlArfaj, E.; Hcini, S.; Mallah, A.; Dhaou, M.H.; Bouazizi, M.L. Effects of Co Substitution on the Microstructural, Infrared, and Electrical Properties of $Mg_{0.6-x}Co_xZn_{0.4}Fe_2O_4$ Ferrites. *J. Supercond. Nov. Magn.* **2018**, *31*, 4107–4116. [CrossRef]

41. Waldron, R.D. Infrared Spectra of Ferrites. *Phys. Rev.* **1955**, *99*, 1727. [CrossRef]

42. Amer, M.A.; Ahmed, M.A.; El-Nimr, M.K.; Mostafa, M.A. Mössbauer and Infrared Studies of the Cu-Cr Ferrites. *Hyperfine Interact.* **1995**, *96*, 91–98. [CrossRef]

43. Shaeel, A.; Al-Thabaiti. *Communications de la Facult ´e des Sciences de l'Universit ´e d'Ankara B*; La Faculté: Leiden, The Netherlands, 2003; Volume 49, pp. 5–14.

44. Mohammed, K.A.; Al-Rawas, A.D.; Gismelseed, A.M.; Sellai, A.; Widatallah, H.M.; Yousif, A.; Elzain, M.E.; Shongwe, M. Infrared and Structural Studies of $Mg_{1-X}Zn_xFe_2O_4$ Ferrites. *Phys. B Condens. Matter* **2012**, *407*, 795–804. [CrossRef]

45. Khalaf, K.A.M.; Al-Rawas, A.D.; Widatallah, H.M.; Al-Rashdi, K.S.; Sellai, A.; Gismelseed, A.M.; Hashim, M.; Jameel, S.K.; Al-Ruqeishi, M.S.; Al-Riyami, K.O. Influence of Zn^{2+} Ions on the Structural and Electrical Properties of $Mg_{1-X}Zn_xFeCrO_4$ Spinels. *J. Alloys Compd.* **2016**, *657*, 733–747. [CrossRef]

46. Yoon, S.J.; Lee, S.H.; Kim, K.H.; Ahn, K.S. Electrical and Magnetic Properties of Spinel $ZnCr_{2-X}Fe_xO_4$ ($0 \leq X \leq 1.0$). *Mater. Chem. Phys.* **2002**, *73*, 330–334. [CrossRef]

47. Pradeep, A.; Priyadharsini, P.; Chandrasekaran, G. Sol–Gel Route of Synthesis of Nanoparticles of $MgFe_2O_4$ and XRD, FTIR and VSM Study. *J. Magn. Magn. Mater.* **2008**, *320*, 2774–2779. [CrossRef]

48. Shokrollahi, H.; Janghorban, K. Soft Magnetic Composite Materials (SMCs). *J. Mater. Process. Technol.* **2007**, *189*, 1–12. [CrossRef]

49. Chakrabarti, P.K.; Nath, B.K.; Brahma, S.; Das, S.; Das, D.; Ammar, M.; Mazaleyrat, F. Magnetic and Hyperfine Properties of Chemically Synthesized Nanocomposites of $(Al_2O_3)_x(Ni_{0.2}Zn_{0.6}Cu_{0.2}Fe_2O_4)_{(1-x)}$ (X = 0.15, 0.30, 0.45). *Solid State Commun.* **2007**, *144*, 305–309. [CrossRef]

50. Modak, S.; Ammar, M.; Mazaleyrat, F.; Das, S.; Chakrabarti, P.K. XRD, HRTEM and Magnetic Properties of Mixed Spinel Nanocrystalline Ni–Zn–Cu-Ferrite. *J. Alloys Compd.* **2009**, *473*, 15–19. [CrossRef]

51. Kambale, R.C.; Shaikh, P.A.; Bhosale, C.H.; Rajpure, K.Y.; Kolekar, Y.D. The Effect of Mn Substitution on the Magnetic and Dielectric Properties of Cobalt Ferrite Synthesized by an Autocombustion Route. *Smart Mater. Struct.* **2009**, *18*, 115028. [CrossRef]

52. Coey, J.M.D. *Rare Earth Permanent Magnetism*; John Wiley and Sons: Hoboken, NJ, USA, 1996. [CrossRef]

53. Patange, S.M.; Shirsath, S.E.; Jadhav, S.S.; Jadhav, K.M. Cation Distribution Study of Nanocrystalline $NiFe_{2-X}Cr_xO_4$ Ferrite by XRD, Magnetization and Mössbauer Spectroscopy. *Phys. Status Solidi* **2012**, *209*, 347–352. [CrossRef]

54. Patange, S.M.; Shirsath, S.E.; Toksha, B.G.; Jadhav, S.S.; Jadhav, K.M. Electrical and Magnetic Properties of Cr^{3+} Substituted Nanocrystalline Nickel Ferrite. *J. Appl. Phys.* **2009**, *106*, 023914. [CrossRef]

55. Néel, L. Magnetism and Local Molecular Field. *Science* **1971**, *174*, 985–992. [CrossRef] [PubMed]

56. Torkian, S.; Ghasemi, A.; Razavi, R.S. Cation Distribution and Magnetic Analysis of Wideband Microwave Absorptive $Co_xNi_{1-X}Fe_2O_4$ Ferrites. *Ceram. Int.* **2017**, *43*, 6987–6995. [CrossRef]

57. Satyanarayana, G.; Nageswara Rao, G.; Babu, K.V.; Santosh Kumar, G.V.; Dinesh Reddy, G. Effect of Cr_{3+} Substitution on the Structural, Electrical and Magnetic Properties of $Ni_{0.7}Zn_{0.2}Cu_{0.1}Fe_{2-x}Cr_xO_4$ Ferrites. *J. Korean Phys. Soc.* **2019**, *74*, 684–694. [CrossRef]